Nano-Structures & Nano-Objects 34 (2023) 100959

Contents lists available at ScienceDirect

Nano-Structures & Nano-Objects

journal homepage: www.elsevier.com/locate/nanoso

Structural and magnetic properties of carbon-encapsulated Fe/Fe_3C nanoparticles

E. Papadopoulou [a], N. Tetos [a], H. Gyulasaryan [b], G. Chilingaryan [b], A. Ginoyan [b], A. Manukyan [b], M. Angelakeris [c], M. Farle [a], M. Spasova [a,*]

[a] Faculty of Physics and Center of Nanointegration (CENIDE), University of Duisburg-Essen, Duisburg, 47057, Germany
[b] Institute for Physical Research of National Academy of Sciences (IPR-NAS), Ashtarak, 0203, Armenia
[c] Physics Department, Aristotle University of Thessaloniki, Greece

ARTICLE INFO

Article history:
Received 16 November 2022
Received in revised form 25 January 2023
Accepted 17 February 2023

Keywords:
Carbon-encapsulated iron-cementite nanoparticles
Solid state pyrolysis
Ferromagnetic nanocomposite

ABSTRACT

Carbon-encapsulated iron-cementite (Fe/Fe_3C) magnetic nanoparticles were synthesized by an up-scalable solid-state pyrolysis method using iron phthalocyanine as a precursor. The dependence of the structure, morphology and magnetic properties on the pyrolysis conditions is presented. The nanocomposite contains nanoparticles made of cementite with a small fraction of iron, with an average diameter of 15 nm embedded in an amorphous carbon matrix.

A 3 nm thick graphite shell is formed on the surface of the particles. The volume fraction of α-Fe increases almost linearly on increasing pyrolysis temperature: from 0.5% for the sample synthesized at 800 °C up to 11% for a 900 °C pyrolysis temperature, resulting in an increase of the saturation magnetization from 14.0 to 17.74 Am^2/kg and a decrease of the coercivity from 49.34 to 10.74 kA/m.

0. Introduction

In the last few decades, magnetic nanoparticles (MNPs) have been of great interest in various science fields. Due to their physicochemical properties, MNPs are found in many technical applications, such as magnetic data storage, catalysis, biomedical theranostics and magnetic ferrofluids [1]. The problems of using magnetic nanoparticles in biomedical applications often are their lack of biocompatibility, chemical inertness and complications in surface functionalization. Biochemical stability and toxicity issues can in principle be overcome by forming core/shell complexes using biocompatible coatings [2]. Aside from biodegradable polymers, organic surfactants and bioactive molecules (liposomes, peptides), shell oxide coatings like silica [3], alumina [4] or carbon [5] have been successfully tested at the laboratory scale. A highlighted option is airtight carbon matrix encapsulation to improve magnetic stability and increase oxidation resistance [6]. Additionally, the carbon shell can decrease the magnetic interactions between the magnetic nanocrystals and enhance their thermal stability [7].

Several forms of iron carbide nanoparticles, such as Fe_2C, $Fe_{2.2}C$, Fe_3C, Fe_5C_2 and Fe_7C_3, have been investigated for applications in magnetic resonance imaging (MRI) [8,9], photothermal therapy (PTT), photoacoustic tomography (PAT) [10] and magnetic particle hyperthermia (MPH) [11,12]. Among these carbides, Fe_3C (cementite), due to its low toxicity, high saturation magnetization (for bulk ~140 A m^2/kg) and chemical stability, is of interest. Fe_3C has an orthorhombic crystal structure and it is ferromagnetic below the Curie temperature (T_C) of 480 K [13]. Since cementite is a metastable phase, the synthesis of pure Fe_3C particles is a challenge and often results in the formation of metallic Fe or mixed Fe and Fe_3C products [14]. This instability of cementite makes it possible to fabricate two-phase nanoparticles with different ratios of iron to cementite by selecting the pyrolysis parameters, thus the magnetic properties can be optimized as required for specific applications.

There are a few reports on the synthesis of Fe/Fe_3C nanoparticles embedded in a carbon matrix, including chemical vapor deposition (CVD), detonation [15], electric plasma discharge [7] and solid-state pyrolysis [16–18] methods. Among them, solid-state pyrolysis offers an advantage due to its simplicity and easy up-scalability, as the properties of the nanoparticles can be controlled by the pyrolysis parameters, e.g. concentration of precursor chemicals, reaction time, temperature and pressure [19,20]. Systematic studies of the influence of pyrolysis parameters on the phase composition, structure and magnetic properties of nanoparticles are still insufficient.

In this work, we present the results of the magnetic and structural characterization of carbon-encapsulated Fe/Fe_3C nanoparticles as a function of the synthesis conditions, that is single step

* Corresponding author.
E-mail address: marina.spasova@uni-due.de (M. Spasova).

https://doi.org/10.1016/j.nanoso.2023.100959
2352-507X/

iron phthalocyanine (Fe-Pc) pyrolysis at different temperatures between 700 and 900 °C (Table 1). The effects of the reaction temperature on the saturation magnetization (M_s), the effective anisotropy constant (K_{eff}), the α-iron content as well as the particle morphology of the Fe/Fe_3C nanocomposites are reported in detail.

1. Materials and method

Composite iron/cementite nanoparticles in a carbon matrix were fabricated by solid state pyrolysis of iron phthalocyanine (FePc, Pc = $C_{32}H_{16}N_8$). A polycrystalline powder of FePc, purified by double sublimation, was used as a precursor which disintegrates at high temperature and simultaneously serves as a source of iron and carbon.

The pyrolysis reaction of iron phthalocyanine for obtaining an iron-based nanocomposite is:

$$Fe\,(N_8C_{32}H_{16}) \xrightarrow[-8H_2,-4N_2]{T_{pyr},\,t_{pyr},\,p} Fe + 32C$$

where T_{pyr} and t_{pyr} are the pyrolysis temperature and time, whilst P is the pressure in the reaction ampoule. The pyrolysis was performed in a sealed quartz glass ampoule with an initial pressure of 0.1 Pa. The volume of the ampoule was ∼80 cm^3 and the weight of the reagent FePc was 150–200 mg. The release of H_2 and N_2 leads to an autogenic pressure in the reactive ampoule of ∼0.7 MPa. The ampoule was placed in a furnace preliminary heated up to T_{pyr} between 700 and 900 °C. After the pyrolysis time, t_{pyr}, the ampoule was rapidly removed from the furnace and cooled down to room temperature. Small iron clusters were formed in contact with a surrounding carbon matrix during the first stages of pyrolysis. Then, with continued growth, the interaction with the matrix leads to the formation of cementite (Fe_3C) at 700 °C [21], according to the following reaction:

$$Fe + 3C \leftrightarrow Fe_3C$$

The backwards reaction corresponds to the thermal decomposition of cementite into elemental iron and a graphitic carbon nanostructure at temperatures above 780 °C [22].

The names of the samples in the article are given according to their pyrolysis temperature. The pyrolysis time for all samples, except those synthesized at the lowest (700 °C) and highest (900 °C) temperatures, was 5 min. The process times for the samples S700 and S900 were 30 and 1200 min, respectively.

2. Characterization

The samples were characterized by X-ray diffraction (XRD) (X'Pert Panalytical diffractometer) employing Cu-K_α radiation ($\lambda = 0.15406\ nm$); $2\theta = 10 - 120°$ at room temperature. Crystalline phases were identified using "Crystallographica Search-Match" software and the "ICDD PDF2" database. To determine crystal cell parameters, crystallite size and phase content, the Rietveld refinement method utilizing the "MAUD" software [23] was used.

Transmission Electron microscopy (TEM) investigations were carried out using a FEI Tecnai F20 TEM/STEM/GIF Supertwin microscope with a field emission gun (FEG) operating at 200 kV, yielding a point resolution of 0.24 nm.

The magnetic measurements were performed on powder samples using a Vibrating Sample Magnetometer (VSM) (Quantum Design PPMS DynaCool). Magnetic hysteresis loops were recorded under magnetic fields of up to ±9 T, in the temperature range from 7 to 300 K.

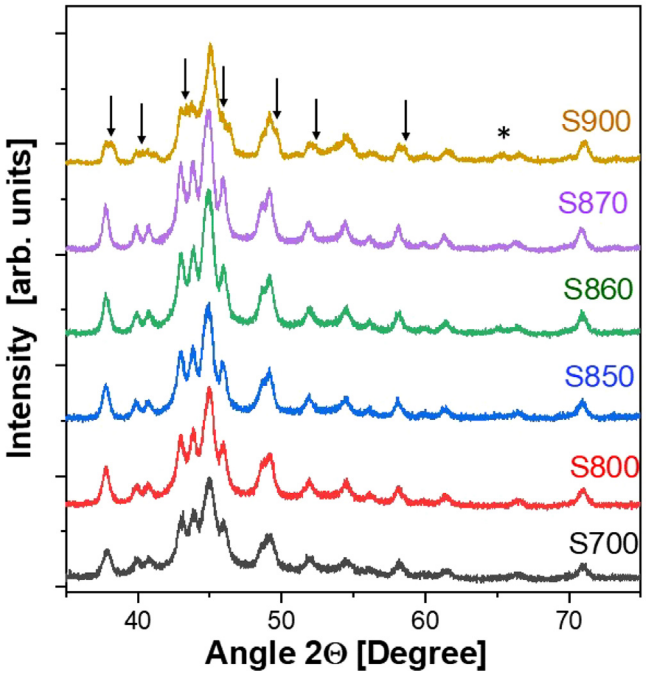

Fig. 1. XRD patterns of the Fe_3C-carbon nanocomposite synthesized by solid state pyrolysis at different temperatures. The (200) α-Fe peak iron is indicated with an asterisk. Additional peaks related to the formation of Fe_5C_2, Fe_4C and γ-Fe phases in S900 are marked by arrows.

3. Results and discussion

3.1. X-ray diffraction

Fig. 1 shows XRD patterns of the samples synthesized at different temperatures. Rietveld refinement of the patterns was performed, suggesting three phases: orthorhombic Fe_3C (*Pnma*, $Z = 4$), hexagonal carbon (*P63/mmc*) and α-Fe (*Im3m*) (Fig. 1S).

The predominant Fe-containing phase is the orthorhombic cementite Fe_3C. The presence of α-Fe is confirmed by the observation of the (200) α-Fe peak at $2\theta = 65.08°$. The (110) α-Fe peak is superimposed with the (031) peak of Fe_3C at $2\theta = 45.02°$. For the sample S900, synthesized at the highest temperature and over a longer time (1020 min), a broadening of the cementite peaks is observed, indicating a decrease in the crystallite size. At the same time, additional peaks appear due to thermal decomposition of Fe_3C, indicating the formation of Fe_5C_2, Fe_4C and γ-Fe phases.

Analysis of the XRD data yields the lattice parameters for the cementite [a = 0.509 ± 0.001 nm, b = 0.675 ± 0.001 nm, c = 0.452 ± 0.001 nm], which are close to those for the bulk orthorhombic Fe_3C phase [24]. The crystallite size and phase content of the nanoparticles (volume fraction of α-Fe and Fe_3C) were determined from the Rietveld refinement of the XRD patterns and the results are summarized in Table 1.

The crystallite size of Fe_3C is 9.5 nm for S700, then it increases up to ∼14 nm for the samples fabricated at temperatures between 800 and 870 °C. A reduction in the coherence length (crystallite size) in the sample synthesized at 900 °C for 1020 min (S900) is observed along with the appearance of new iron-bearing phases, indicating that the new phases are formed due to the partial thermal disintegration of Fe_3C inside the crystalline grains.

The volume fraction of α-Fe increases almost linearly on increasing the pyrolysis temperature: from 0.5% for the sample synthesized at 800 °C up to 11% for the 900 °C pyrolysis temperature. No evidence for Fe oxide formation is seen, outlining the role of the graphite protective MNP coating.

Table 1
Structural and phase analysis of the XRD data for the Fe_3C-carbon nanocomposites fabricated with different pyrolysis parameters: temperature, T_{pyr}, and time, t_{pyr}.

Sample	Pyrolysis temperature, $T_{pyr,r}$, [°C]	Pyrolysis time, t_{pyr} [min]	Crystallite size of Fe_3C, [nm]	Volume fraction of α-Fe, [%]
S700	700	30	9.5 ± 0.7	–
S800	800	5	13.8 ± 0.7	0.4 ± 0.1
S850	850	5	13.1 ± 1.3	3.6 ± 0.7
S860	860	5	13.8 ± 0.8	6.1 ± 1.7
S870	870	5	15.7 ± 3.4	3.6 ± 2.1
S900	900	1020	9.5 ± 1.3	11.0 ± 0.3

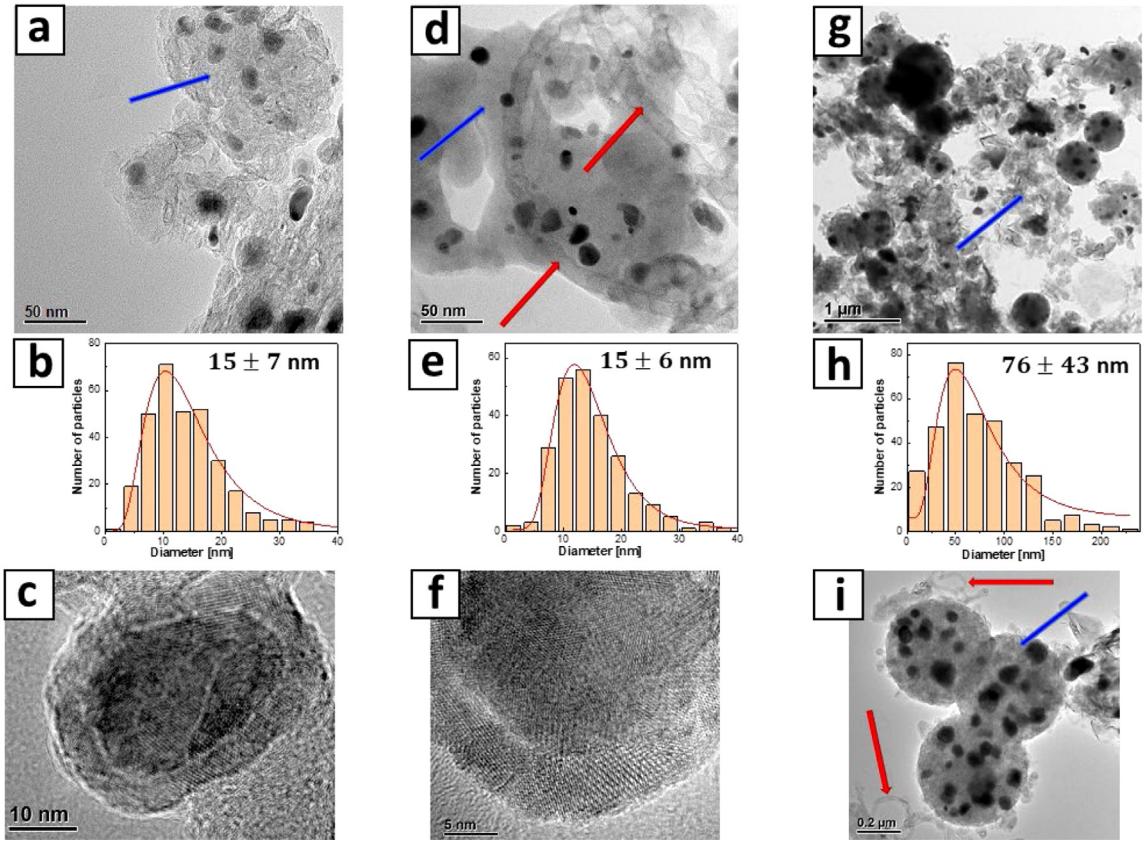

Fig. 2. TEM/HRTEM images and particle size distribution histograms for Fe_3C-carbon composites synthesized at 700 (a–c), 850 (d–f) and 900 °C (g–i). The distribution of the Fe_3C nanoparticle size was fitted using a lognormal function. Amorphous areas of the carbon matrix are indicated by blue arrows, multiwall carbon nanotubes by red ones. . (For interpretation of the references to color in this figure legend, the reader is referred to the web version of this article.)

3.2. Transmission electron microscopy

Fig. 2 shows TEM and High Resolution TEM (HRTEM) images together with particle size distribution histograms for the Fe_3C-carbon nanocomposites synthesized at 700, 850 and 900 °C.

Nanoparticles with an average diameter of 15 nm with a standard deviation of ∼50%, embedded in a polymorphous carbon matrix are formed at the pyrolysis temperature 700 °C $\leq T_{pyr} \leq$ 870 °C. Particles with diameters smaller than 15 nm are single crystalline. This observation is in full agreement with the XRD results. The particles exhibit a well defined core–shell morphology: a Fe_3C core surrounded by ∼3–4 nm thick crystalline graphite shell. High Resolution TEM images confirm the Fe_3C phase. The carbon matrix consists of amorphous carbon with some amount of carbon nanotubes. The increase of the pyrolysis temperature combined with a substantially increased pyrolysis time results in the formation of carbon spheres of 200–700 nm diameter with embedded Fe_3C nanoparticles. The size of the Fe-containing particles becomes significantly larger and reaches 80 nm (Fig. 2g–i).

3.3. Magnetic properties

Magnetization measurements were performed at different temperatures between 10 and 300 K. The maximum field applied was ±9 T. Fig. 3 shows the magnetization versus external applied field loops recorded at 10 and 300 K for the samples fabricated at 850 and 900 °C. The M(H) curves show a typical ferromagnetic behavior, where the saturation magnetization, the remanent magnetization and the coercive field decrease with increasing temperature.

Magnetic data for the Fe_3C-carbon nanocomposites are summarized in Table 2.

The saturation magnetization of the Fe/Fe_3C-carbon nanocomposite material increases as the pyrolysis temperature increases, while the coercive field gradually decreases. The remanence to saturation ratio ($\frac{M_{rem}}{M_s}$), close to 0.5, is measured at low temperature for the samples synthesized in the temperature range from 800 to 870 °C, as theoretically predicted by the Stoner–Wohlfarth model for an array of randomly oriented single domain non-interacting particles with uniaxial magnetic anisotropy.

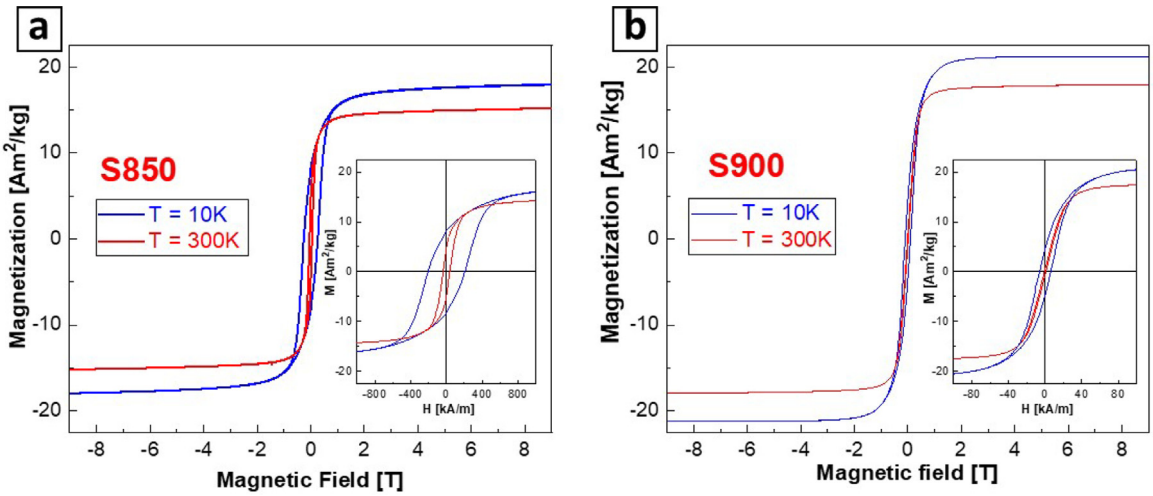

Fig. 3. Field dependence of the magnetization for the samples fabricated at 850 (S850) and 900 °C (S900), recorded at 10 and 300 K. The insets show the low field region of the hysteresis loops.

Table 2
Saturation magnetization M_s, ratio of remanent to the saturation magnetization $\frac{M_{rem}}{M_s}$ and coercive field strength H_c measured at 10 and 300 K.

Sample	M_s (10 K) $\left[\frac{\text{A m}^2}{\text{kg}}\right]$	$\frac{M_{rem}}{M_s}$ (10 K)	H_c (10 K) $\left[\frac{\text{kA}}{\text{m}}\right]$	M_s (300 K) $\left[\frac{\text{A m}^2}{\text{kg}}\right]$	$\frac{M_{rem}}{M_s}$ (300 K)	H_c (300 K) $\left[\frac{\text{kA}}{\text{m}}\right]$
S700				12.4	0.25	17.5
S800	17.9	0.46	205.3	14.0	0.38	49.34
S850	18.0	0.46	196.5	14.8	0.32	37.40
S860	19.4	0.48	174.3	15.9	0.30	30.24
S870	19.7	0.47	167.1	16.6	0.28	29.44
S900	21	0.22	76.4	17.74	0.03	10.74

The lowering of $\frac{M_{rem}}{M_s}$ at 300 K points to the fact that a certain fraction of the nanoparticles turns into a zero-remanence superparamagnetic state.

The upper limit for the single-domain state for the nanoparticle diameter can be estimated as $d_{SD} = \frac{18\sigma^{180°}}{\mu_0 M_s^2}$ [25], where $\sigma^{180°} = \pi\sqrt{AK}$ is a 180° domain energy density with A being the exchange stiffness constant and K being the magnetic anisotropy energy constant. Using the values for bulk cementite ($A = 8.7 \times 10^{-12}$ $\frac{\text{J}}{\text{m}}$ [26], $K \approx 2 \times 10^5$ $\frac{\text{J}}{\text{m}^3}$ [27], $M_s \approx 1.03 \times 10^6$ $\frac{\text{A}}{\text{m}}$ [28], we obtained 56 nm as the upper diameter limit for the single-domain state.

The sample S900 shows a significant decrease in the remanent magnetization, revealing the multi-domain nature of the magnetic particles in this sample, which, in fact, is expected from the much bigger average size as outlined by the TEM analysis.

The temperature dependent decay of the coercive field with increasing temperature in an array of the magnetic nanoparticles is described by Kneller's law [29]:

$$H_c(T) = H_{ci}\left(1 - \left(\frac{T}{T_B}\right)^{\alpha_K}\right). \quad (1)$$

Here H_{ci} is the intrinsic coercivity at T = 0 K, T_B is the superparamagnetic blocking temperature and α_K is Kneller's exponent. A fit according to Eq. (1) yields the intrinsic coercivity $H_{ci} = 217.5$ and 181.6 $\frac{\text{kA}}{\text{m}}$ for samples S850 and S870, respectively. $T_B = 365$ K and $\alpha_K = 0.83$ were obtained for both samples. It should be noted that below the blocking temperature, the Kneller's exponent is expected to be 0.5 for an array of non-interacting single-domain nanoparticles with uniaxial anisotropy. The difference of our result to the model can be explained by the non-uniformity of the particle size [29]. Due to the broad particle size distribution of the Fe_3C-carbon nanocomposites, one has to consider the presence of superparamagnetic nanoparticles besides thermally stable single-domain ones. The fraction of "zero coercivity" nanoparticles, ϵ, can be obtained from the ratio of remanent to saturation magnetization $\frac{M_r}{M_s} = r(1-\epsilon)$. The numerical factor r depends on the alignment of the nanoparticles and their symmetry and it is equal to 0.5 for randomly oriented uniaxial ones. An increasing fraction of superparamagnetic nanoparticles with increasing temperature (Fig. 4b) modifies the Kneller's exponent.

To determine the effective magnetocrystalline anisotropy, the reversible parts of the isothermal M(H) data for the Fe_3C-carbon nanocomposites in the field range from 1.2 up to 4 MA/m were fitted by the law of approach to saturation (LAS) for a polycrystalline material with uniaxial anisotropy [30,31] (Fig. 3S in Supplementary Information)

$$M(H) = M_s\left[1 - \frac{1}{15}\left(\frac{H_A}{H}\right)^2\right] + \chi H, \quad (2)$$

where M_s is the saturation magnetization, H_A is the anisotropy field, χ is the paramagnetic susceptibility.

The effective magnetocrystalline anisotropy is given by $K = \frac{1}{2}\mu_0 M_V^{FM} H_A$ (μ_o is the permeability of free space and M_V^{FM} is the volume magnetization of the ferromagnetic component of the nanocomposite).

Fig. 5 shows the temperature dependence of the effective anisotropy constant K and the mass saturation magnetization M of the nanocomposites synthesized at 850 and 870 °C.

The saturation magnetization and the anisotropy constant decrease with increasing temperature, which is typical behavior for ferromagnetic materials. The saturation magnetization is higher for the sample synthesized at a higher temperature, while the anisotropy constant is lower. This is due to the increase of the magnetically soft iron fraction with higher magnetization. The

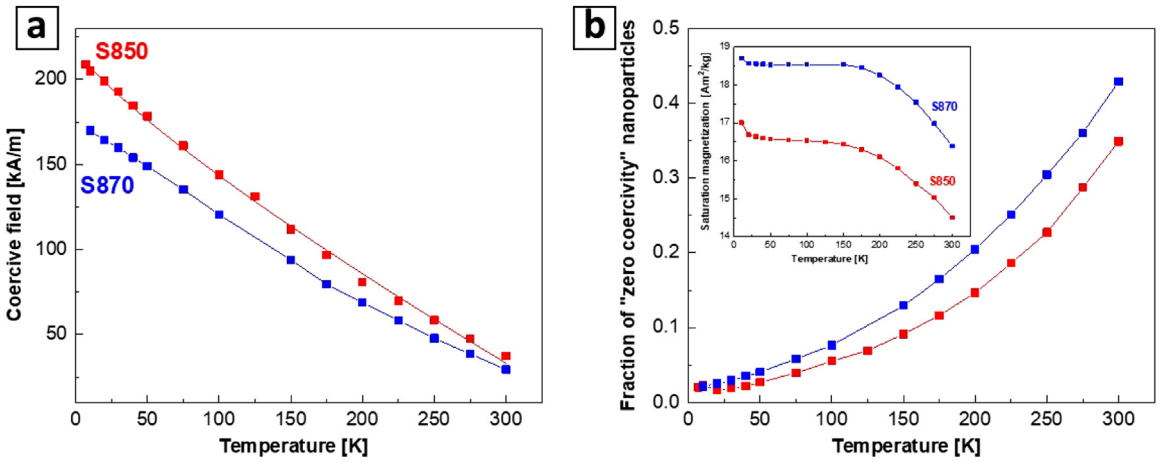

Fig. 4. (a) Temperature dependence of the coercive field for samples S850 and S870. Lines are fits according to Eq. (1). (b) Fraction of the "zero remanence" "zero coercivity" nanoparticles versus temperature. Inset shows the temperature dependence of the saturation magnetization of the samples.

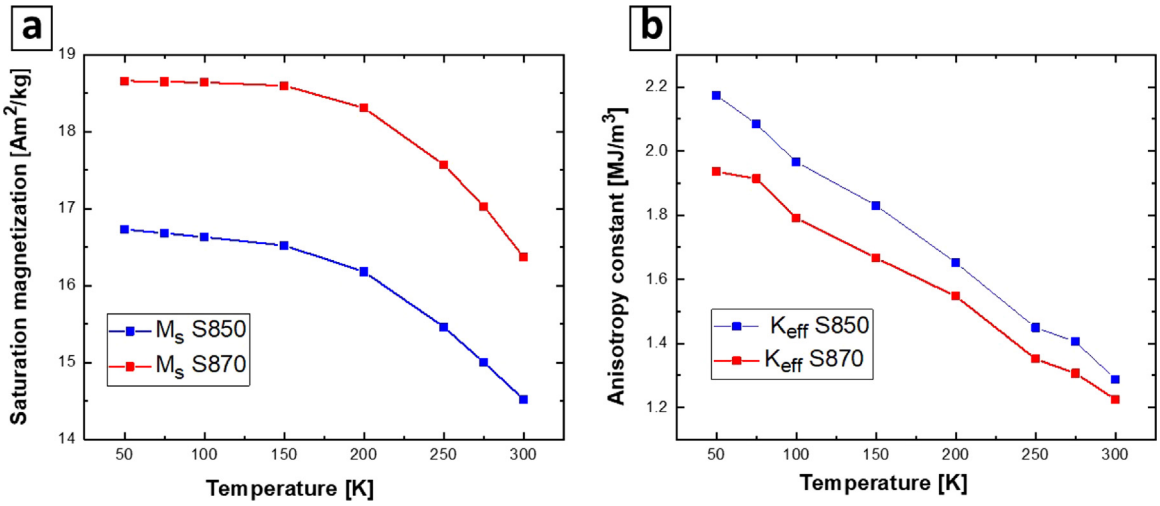

Fig. 5. Temperature dependence of the effective anisotropy constant (a) and mass saturation magnetization obtained from the fit of the experimental values M(H) by LAS (Eq. (2)).

value of the anisotropy constant is approximately one order larger in comparison to that of bulk cementite. We attribute this to the contribution of the surface anisotropy, magnetostriction effects and/or deviation from the spherical shape in the nanoparticle system [32,33].

4. Conclusion

Fe-containing nanoparticle–carbon composites were fabricated by a simple and up-scalable solid state pyrolysis of iron phthalocyanine at different temperatures and time. The resulting material is iron-containing nanoparticles with an average diameter of 15 nm embedded in an amorphous carbon matrix. A 3 nm thick graphite shell is formed on the surface of the particles. The nanoparticles are mainly composed of cementite with a small amount of iron, the amount of which increases on increasing the synthesis temperature (Table 1). This results in an increase of the saturation magnetization and a decrease of the effective magnetic anisotropy constant for the composites (Table 2). Increasing the synthesis time also results in the growth of the nanoparticle diameter, as outlined by the 200–600 nm diameter carbon nanospheres with embedded magnetic nanoparticles.

CRediT authorship contribution statement

E. Papadopoulou: Investigation, Writing – original draft. **N. Tetos:** Investigation. **H. Gyulasaryan:** Investigation. **G. Chilingaryan:** Investigation. **A. Ginoyan:** Investigation. **A. Manukyan:** Supervision, Conceptualization, Methodology, Writing – review & editing. **M. Angelakeris:** Supervision, Writing – review & editing. **M. Farle:** Supervision, Writing – review & editing. **M. Spasova:** Conceptualization, Methodology, Investigation, Writing – original draft, Writing – review & editing.

Declaration of competing interest

The authors declare that they have no known competing financial interests or personal relationships that could have appeared to influence the work reported in this paper.

Data availability

Data will be made available on request.

Acknowledgment

This work was supported by the European Union's Horizon 2020 research and innovation programme under grant agreement No 857502 (MaNaCa).

Appendix A. Supplementary data

Supplementary material related to this article can be found online at https://doi.org/10.1016/j.nanoso.2023.100959.

References

[1] A.-H. Lu, E.L. Salabas, F. Schüth, Magnetic nanoparticles: synthesis, protection, functionalization, and application, Angew. Chem. Int. Ed. Engl. 46 (2007) 1222–1244, http://dx.doi.org/10.1002/anie.200602866.

[2] V. Davydov, A. Rakhmanina, I. Kireev, I. Alieva, O. Zhironkina, O. Strelkova, V. Dianova, T.D. Samani, K. Mireles, L. Yahia, R. Uzbekov, V. Agafonov, V. Khabashesku, Solid state synthesis of carbon-encapsulated iron carbide nanoparticles and their interaction with living cells, J. Mater. Chem. B 2 (2014) 4250–4261, http://dx.doi.org/10.1039/C3TB21599G.

[3] P.-L. Liu, Y.-P. Xu, P. Zheng, H.-W. Tong, Y.-X. Liu, Z.-G. Zha, Q.-D. Su, S.-M. Liu, Mesoporous silica-coated magnetic nanoparticles for mixed hemimicelles solid-phase extraction of phthalate esters in environmental water samples with liquid chromatographic analysis, J. Chin. Chem. Soc. 60 (2013) 53–62, http://dx.doi.org/10.1002/jccs.201200096.

[4] F. Jay, V. Gauthier, S. Dubois, Iron particles coated with alumina: Synthesis by a mechanofusion process and study of the high-temperature oxidation resistance, J. Am. Ceram. Soc. 89 (2006) 3522–3528, http://dx.doi.org/10.1111/j.1551-2916.2006.01266.x.

[5] V.I. Shubayev, T.R. Pisanic, S. Jin, Magnetic nanoparticles for theragnostics, Adv. Drug Deliv. Rev. 61 (2009) 467–477, http://dx.doi.org/10.1016/j.addr.2009.03.007.

[6] A. Wu, D. Liu, L. Tong, L. Yu, H. Yang, Magnetic properties of nanocrystalline Fe/Fe_3C composites, CrystEngComm 13 (2011) 876–882, http://dx.doi.org/10.1039/C0CE00328J.

[7] R. Sergiienko, E. Shibata, Z. Akase, H. Suwa, T. Nakamura, D. Shindo, Carbon encapsulated iron carbide nanoparticles synthesized in ethanol by an electric plasma discharge in an ultrasonic cavitation field, Mater. Chem. Phys. 98 (2006) 34–38, http://dx.doi.org/10.1016/j.matchemphys.2005.08.064.

[8] W. Tang, Z. Zhen, C. Yang, L. Wang, T. Cowger, H. Chen, T. Todd, K. Hekmatyar, Q. Zhao, Y. Hou, J. Xie, Fe_5c_2 nanoparticles with high MRI contrast enhancement for tumor imaging, Small 10 (2014) 1245–1249, http://dx.doi.org/10.1002/smll.201303263.

[9] G. Huang, J. Hu, H. Zhang, Z. Zhou, X. Chi, J. Gao, Highly magnetic iron carbide nanoparticles as effective T(2) contrast agents, Nanoscale 6 (2014) 726–730, http://dx.doi.org/10.1039/c3nr04691e.

[10] J. Yu, C. Yang, J. Li, Y. Ding, L. Zhang, M.Z. Yousaf, J. Lin, R. Pang, L. Wei, L. Xu, F. Sheng, C. Li, G. Li, L. Zhao, Y. Hou, Multifunctional fe_5c_2 nanoparticles: a targeted theranostic platform for magnetic resonance imaging and photoacoustic tomography-guided photothermal therapy, Adv. Mater. 26 (2014) 4114–4120, http://dx.doi.org/10.1002/adma.201305811.

[11] M. Angelakeris, Magnetic nanoparticles: A multifunctional vehicle for modern theranostics, Biochim. Biophys. Acta (BBA) 1861 (2017) 1642–1651, http://dx.doi.org/10.1016/j.bbagen.2017.02.022.

[12] A. Rajan, N.K. Sahu, Review on magnetic nanoparticle-mediated hyperthermia for cancer therapy, J. Nanopart. Res. 22 (2020) 1–25, http://dx.doi.org/10.1007/s11051-020-05045-9.

[13] H.K.D.H. Bhadeshia, Cementite, Int. Mater. Rev. 65 (2020) 1–27, http://dx.doi.org/10.1080/09506608.2018.1560984.

[14] Z. Schnepp, S.C. Wimbush, M. Antonietti, C. Giordano, Synthesis of highly magnetic iron carbide nanoparticles via a biopolymer route, Chem. Mater. 22 (2010) 5340–5344, http://dx.doi.org/10.1021/cm101746z.

[15] N. Luo, X. Li, X. Wang, H. Yan, C. Zhang, H. Wang, Synthesis and characterization of carbon-encapsulated iron/iron carbide nanoparticles by a detonation method, Carbon 48 (2010) 3858–3863, http://dx.doi.org/10.1016/j.carbon.2010.06.051.

[16] R. Kumar, R. Rajendiran, H.K. Choudhary, N.K. GM, B. Balaiah, A.A. V, B. Sahoo, Role of pyrolysis reaction temperature and heating-rate in the growth and morphology of carbon nanostructures, Nano-Struct. Nano-Objects 12 (2017) 229–238, http://dx.doi.org/10.1016/j.nanoso.2017.11.002.

[17] B.K. Barman, K.K. Nanda, Prussian blue as a single precursor for synthesis of Fe/Fe_3c encapsulated N-doped graphitic nanostructures as bi-functional catalysts, Green Chem. 18 (2016) 427–432, http://dx.doi.org/10.1039/C5GC01405K.

[18] L. Avakyan, A. Manukyan, A. Bogdan, H. Gyulasaryan, J. Coutinho, E. Paramonova, G. Sukharina, V. Srabionyan, E. Sharoyan, L. and Bugaev, Synthesis and structural characterization of iron-cementite nanoparticles encapsulated in carbon matrix, J. Nanopart. Res. 22 (2020) http://dx.doi.org/10.1007/s11051-019-4698-8.

[19] G. Tong, Y. Liu, F. Liu, J. Guan, Easy gas-flow-induced CVD synthesis and tunable electromagnetic characteristics of centipede-shaped iron/cementite/multiwalled carbon nanotube (Fe/Fe_3c/MWCNT) heterostructures, Surf. Coat. Technol. 283 (2015) 286–297, http://dx.doi.org/10.1016/j.surfcoat.2015.10.058.

[20] D. Kuang, L. Hou, S. Wang, H. Luo, L. Deng, J. He, M. Song, Facile synthesis of Fe/Fe_3C-C core–shell nanoparticles as a high-efficiency microwave absorber, Appl. Surf. Sci. 493 (2019) 1083–1089, http://dx.doi.org/10.1016/j.apsusc.2019.07.073.

[21] C. Giordano, A. Kraupner, S.C. Wimbush, M. Antonietti, Iron carbide: an ancient advanced material, Small 6 (2010) 1859–1862, http://dx.doi.org/10.1002/smll.201000437.

[22] D. Chaira, B.K. Mishra, S. Sangal, Efficient synthesis and characterization of iron carbide powder by reaction milling, Powder Technol. 191 (2009) 149–154, http://dx.doi.org/10.1016/j.powtec.2008.09.020.

[23] L. Lutterotti, S. Matthies, H.R. Wenk, MAUD (material analysis using diffraction): a user friendly java program for rietveld texture analysis and more, 1999.

[24] I.G. Wood, L. Vočadlo, K.S. Knight, D.P. Dobson, W.G. Marshall, G.D. Price, J. and Brodholt, Thermal expansion and crystal structure of cementite, fe_3C, between 4 and 600 K determined by time-of-flight neutron powder diffraction, J. Appl. Crystallogr. 37 (2004) 82–90, http://dx.doi.org/10.1107/S0021889803024695.

[25] S. Blundell, Magnetism in Condensed Matter, Oxford University Press, Oxford, 2001.

[26] D. Liu, J. Zhu, S. Ivaturi, Y. He, S. Wang, J. Wang, S. Zhang, M.A.C. Willis, F.S. Boi, Giant magnetic coercivity in fe_3C-filled carbon nanotubes, RSC Adv. 8 (2018) 13820–13825, http://dx.doi.org/10.1039/c7ra13671d.

[27] S. Yamamoto, T. Terai, T. Fukuda, K. Sato, T. Kakeshita, S. Horii, M. Ito, M. Yonemura, Magnetocrystalline anisotropy of cementite pseudo single crystal fabricated under a rotating magnetic field, J. Magn. Magn. Mater. 451 (2018) 1–4, http://dx.doi.org/10.1016/j.jmmm.2017.10.114.

[28] B. Kaeswurm, K. Friemert, M. Gürsoy, K.P. Skokov, O. Gutfleisch, Direct measurement of the magnetocaloric effect in cementite, J. Magn. Magn. Mater. 410 (2016) 105–108, http://dx.doi.org/10.1016/j.jmmm.2016.02.080.

[29] E.F. Kneller, F.E. Luborsky, Particle size dependence of coercivity and remanence of single-domain particles, J. Appl. Phys. 34 (1963) 656–658, http://dx.doi.org/10.1063/1.1729324.

[30] N.S. Akulov, Über den verlauf der magnetisierungskurve in starken feldern, Z. Phys. 69 (1931) 822–831, http://dx.doi.org/10.1007/BF01339465.

[31] J.F. Herbst, F.E. Pinkerton, Law of approach to saturation for polycrystalline ferromagnets: Remanent initial state, Phys. Rev. B 57 (1998) 10733–10739, http://dx.doi.org/10.1103/physrevb.57.10733.

[32] L. Berger, Y. Labaye, M. Tamine, J.M.D. Coey, Ferromagnetic nanoparticles with strong surface anisotropy: Spin structures and magnetization processes, Phys. Rev. B 77 (2008) http://dx.doi.org/10.1103/physrevb.77.104431.

[33] D. Lisjak, A. Mertelj, Anisotropic magnetic nanoparticles: A review of their properties, syntheses and potential applications, Prog. Mater. Sci. 95 (2018) 286–328, http://dx.doi.org/10.1016/j.pmatsci.2018.03.003.